buildings

MDPI

Article

Building-Integrated Solar Delivery Strategies for Algae Photobioreactors in Cold Climates

Neda Ghaeili Ardabili, Mohammad Elmi and Julian Wang *

Department of Architectural Engineering, Pennsylvania State University, State College, PA 16802, USA; nxg51@psu.edu (N.G.A.); mke5304@psu.edu (M.E.)
* Correspondence: julian.wang@psu.edu

Abstract

Microalgae photobioreactors (PBRs) are promising building-integrated biotechnologies for carbon capture and biomass production; however, their high energy requirements for artificial lighting remain a significant energy barrier in cold climates. This study developed an integrated spectral–optical energy modeling framework to evaluate two PBR deployment strategies in State College, PA: rooftop daylight-exposed integration and basement installation with solar-assisted lighting. Results show that fiber-optic daylighting can supply a substantial fraction of photosynthetically useful light without introducing additional internal heat loads, while photovoltaics sized at approximately 0.40–0.55 kWDC per reactor can offset the annual PBR lighting energy use when sufficient roof area is available. Whole-building energy simulations further reveal that rooftop PBR integration reduces total annual space energy consumption by ~21% relative to basement placement due to lower artificial lighting and cooling loads. When combined, PV and fiber systems can fully meet basement PBR lighting demand, whereas rooftop configurations may rely more on grid electricity. Economically, fiber-optic daylighting achieves comparable lighting offsets at roughly half the annualized cost of PV-based systems, subject to surface-area and routing constraints. Overall, solar-assisted lighting strategies markedly improve the operational sustainability of building-integrated PBRs in cold climates, with fiber-optic daylighting offering substantial spectral and thermal advantages, subject to surface-area availability and routing-related design constraints.

Keywords: sustainable biomass systems; building-integrated photobioreactor; light-guiding fiber; photovoltaic integration; cold climate building systems

Check for updates

Academic Editor: Chi Yan Tso

Received: 16 December 2025
Revised: 12 January 2026
Accepted: 12 January 2026
Published: 17 January 2026

Copyright: © 2026 by the authors. Licensee MDPI, Basel, Switzerland. This article is an open access article distributed under the terms and conditions of the Creative Commons Attribution (CC BY) license.

1. Introduction

About 39% of energy-related greenhouse gas emissions (GHG) and nearly a third of total global energy consumption are attributed to buildings [1]. Increasing energy demand, embodied carbon in materials, and concerns over indoor environmental quality have prompted an urgent need to redefine how buildings interact with the environment. A conventional design approach that focuses primarily on operational efficiency is becoming insufficient to achieve net-zero or net-positive performance targets. This has led to increased interest in bio-integrated, smart, and adaptive building paradigms that can reduce carbon emissions, recycle resources, and contribute to ecological resilience. Within this context, bio-integrated façade and interior systems, such as microalgae PBRs, offer a novel pathway to transform buildings from passive energy consumers into active participants in circular and carbon-negative ecosystems [2–4]. Based on this vision, researchers have

increasingly focused on integrating biological systems into the built environment to promote renewable energy production and sustainable bioresource generation. Among these, microalgae PBRs have emerged as promising bio-integrated technologies capable of carbon capture, wastewater treatment, and biofuel generation while simultaneously contributing to improved indoor air quality and biophilic design objectives in buildings [5–7]. Due to their rapid growth rate, high photosynthetic efficiency, and controllability, they are particularly suitable for use in urban areas and circular bioeconomy strategies [8]. Several studies have focused on implementing the PBR or biomass production to improve building energy performance. For example, ref. [9] demonstrated that in a cold, semi-arid climate, building-integrated microalgae PBR façades can significantly reduce energy consumption and enhance daylight performance, with optimization showing up to a 40% improvement in energy efficiency compared to conventional glazing systems. Ref. [10] demonstrated that integrating photobioreactors as algae windows can significantly enhance building sustainability by reducing cooling loads, improving daylight quality, and enabling hot-water generation, highlighting their multifunctional potential for energy efficiency, carbon mitigation, and indoor environmental improvement. Another recent work emphasized the potential of algae-integrated façades as nature-inspired technologies capable of simultaneously producing biomass and energy, treating wastewater, and enhancing building thermal and acoustic performance, demonstrating algae building technology as a viable pathway toward a more sustainable future [2]. Furthermore, experimental and simulation-based research has also shown that algae bio-reactive building envelopes can function as self-adaptive shading systems, dynamically regulating daylight and heat while simultaneously enabling solar energy harvesting and CO_2 capture in urban environments [11].

However, these studies primarily evaluated the architectural or environmental performance of algae façades while neglecting the energy required for algae cultivation itself, including artificial lighting, aeration, and temperature regulation, which critically affects real-world efficiency. These operational demands significantly influence system feasibility, yet they remain insufficiently addressed in the current literature. As a result, despite their conceptual advantages, building-integrated PBRs remain limited in real-world adoption and deployment, particularly in cold regions such as the Northeastern United States, where artificial lighting and thermal conditioning impose considerable additional energy burdens [12]. Light availability determines algal productivity; in closed PBRs, photon flux densities in the 400–700 nm range are required to sustain growth. Often, this situation is achieved through continuous LED illumination [4,13]. Studies on algae or PBR operation in cold climates suggest that artificial illumination becomes the dominant electricity end-use in winter, often exceeding the operating energy demands observed in warmer regions with higher daylight availability [14,15]. Recent advances in solar energy engineering offer new opportunities to address these challenges. With optical-fiber daylighting and light-guiding systems, sunlight is channeled into enclosed reactors while preserving its spectral integrity [16]. Moreover, photovoltaic technologies can be employed to generate on-site renewable electricity for lighting and control systems, thus reducing grid dependence.

A conceptual overview of the integrated system, including the solar light-guiding, PBR, and photovoltaic modules, is illustrated in Figure 1. This figure shows how collected solar radiation is split and directed through optical fibers to the PBR, while PV panels capture surplus energy for lighting and control operations.

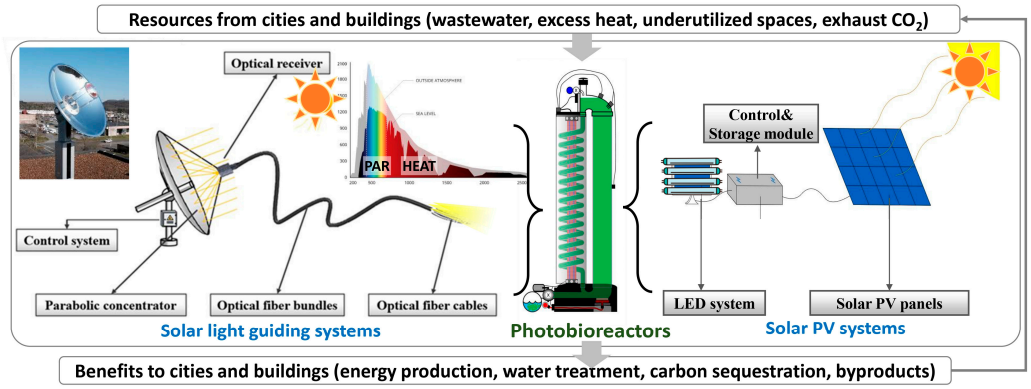


Figure 1. Conceptual schematic of the integrated solar–PBR–PV system showing the solar light-guiding subsystem, PBR module, and photovoltaic energy unit.

Despite significant progress in the individual study of daylighting systems, algal PBRs, and building energy simulations, the quantitative relationships among solar spectral availability, optical transmission efficiency, algal photosynthetic response, and building-scale energy performance have not yet been thoroughly investigated, particularly for northern climate applications. In such regions, lower solar irradiance, frequent cloud cover, and shorter daylight hours introduce complex interactions between the optical behavior of light-guiding systems, the spectral requirements of photosynthetic organisms, and the dynamic energy balance of buildings. Understanding these coupled effects is essential for developing reliable design strategies and accurately predicting the overall performance of integrated PV and PBR systems in real-world environments.

To bridge this gap, the present study develops a multi-scale modeling framework linking (1) optical-fiber transmittance analysis, (2) species-weighted photosynthetic evaluation, and (3) building-level PV–PBR energy simulation. Using *Chlorella vulgaris* as a model species, the study compares two integration scenarios within a prototypical mid-rise residential building in State College, Pennsylvania: (i) Installation relying solely on LED illumination, and (ii) rooftop integration with fiber-guided sunlight and LED supplementation. This research has four objectives. First, the study aims to analyze the spectral and optical performance of solar-transmission fibers under actual annual sky conditions to determine how effectively they deliver photosynthetically usable radiation (PUR) to enclosed photobioreactors. Second, it aims to quantify the amount of PUR that reaches the algae culture, evaluating how effectively natural and guided sunlight support microalgal growth. Third, the research evaluates the potential of on-site photovoltaic (PV) systems to generate sufficient renewable electricity to offset the lighting energy demand required for PBR operation. Finally, the study examines the overall building energy impacts of integrating these systems in a building under two different scenarios: rooftop-integrated versus basement configurations. This analysis aims to identify the most efficient and sustainable design strategies for cold-climate applications.

2. Methods

Multi-stage modelling and acquisition were employed in the study. In total, the process integrates five steps of solar spectral power distribution (SPD) extraction, optical fiber transmittance-based daylight estimation, PV generation assessment, algae PBR modelling, and whole-building energy simulation.

2.1. Solar SPD Modeling

The spectral solar data required for the optical daylight and energy modeling were generated using the Bird Simple Spectral Model [17]. As summarized in Table 1 the

spreadsheet was parameterized using the geographic coordinates of State College, PA (40.8° N, 77.9° W) and the corresponding solar geometry for three representative seasonal days: the summer solstice (Day 172), the equinox (Day 265), and the winter solstice (Day 355). These days were selected to capture the annual variation in solar altitude and daylight availability. For each representative day, two sky conditions, clear and cloudy, were considered. Annual sky conditions were subsequently reconstructed by weighting the SPDs according to the annual ratio of cloudy to clear skies. In the spreadsheet, sky condition is defined solely through the aerosol optical depth (AOD), following [18]. The maximum measurable AOD is 3. Based on typical ranges reported in the literature, clear-sky conditions were assumed to correspond to AOD values of 0.05–0.5, while AOD values of 1.8–3 represented cloudy-sky conditions. The mean value of each range was used to define the representative sky states. Accordingly, AOD values of 0.3 and 2.4 were adopted to represent clear and cloudy skies, respectively. The surface angle was set to −1 to define a surface continuously tracking the sun's path, remaining perpendicular to the solar rays throughout the day. The model outputs the SPD of global, direct, and diffuse solar irradiance in units of $W \cdot m^{-2} \cdot nm^{-1}$, from which the direct solar irradiance SPD was extracted and used for all further assessments and calculations. As mentioned, for the annual calculation, hourly sky conditions were extracted from the EPW file to weight the representative days by the clear-cloudy ratio and capture its influence on seasonal solar gradients, ensuring a realistic annual sky-condition profile rather than relying on fully clear or fully cloudy assumptions. For this reason, hours with total sky cover $\geq$5/10 were classified as cloudy, and cloudy-condition DNI values were applied. Hours with sky cover <5/10 were classified as clear, and clear-sky DNI values were used. According to the State College EPW file, the proportion of cloudy daylight hours across each season was 55% in summer, 66% during the spring and fall period represented by the equinox, and 65% in winter. These seasonal cloudiness ratios were then used to scale the solstice and equinox spectral outputs by the number of days in each season, yielding annual predictions. This classification ensured that hourly spectral inputs to the fiber-optic transmission model reflected real variations in sky condition rather than relying solely on idealized clear- or cloudy-sky assumptions.

Table 1. Input variables used to define sky conditions.

Latitude	Longitude	NDay	AOD	Fix Tilt
40.79°	−77.86°	172, 265, 355	0.3, 2.4	−1° (assuming the sun tracking surface)

The direct solar irradiance was extracted and implemented as the fundamental inputs for subsequent stages of analysis: (i) to evaluate optical fiber transmittance-based daylight estimation, quantifying how much of the solar spectrum is transmitted through the fibers to the reactor plane; and (ii) to compute algae species-weighted PAR and PPFD values, enabling wavelength-specific assessment of photosynthetic light-use efficiency. The resulting SPDs thus provide a direct spectral link between the external solar environment and the PBR's internal lighting conditions.

2.2. Optical Fiber Daylighting Modelling

Optical fiber daylighting systems are innovative technologies that capture, transmit, and distribute natural sunlight through flexible optical fibers, enabling efficient delivery of daylight to interior or enclosed environments. These systems generally consist of three functional stages: (1) a solar collector that concentrates and couples sunlight into the fiber,

(2) optical fibers that transmit light through total internal reflection, and (3) luminaires or diffusers that distribute the transmitted light to the target space.

Optical fiber systems use a core–cladding structure to deliver light via total internal reflection efficiently. In contrast to conventional light-pipe or mirror-based daylighting systems, optical fiber systems offer greater routing flexibility, improved spectral selectivity, and higher luminous efficiency over long distances [19,20].

The ability of optical fibers to maintain the spectral fidelity of transmitted sunlight makes them particularly valuable for applications requiring controlled spectral quality, such as indoor agriculture, algae cultivation, and building-integrated bioreactors [21]. In these contexts, optical fibers can selectively transmit PAR (400–700 nm) to optimize biological productivity while minimizing the need for energy-intensive artificial lighting. Several recent studies have demonstrated the feasibility of fiber-based solar transport for supporting biological growth and carbon capture. For instance, Song et al. [22] showed that optical fiber and light-guide tube systems can significantly enhance carbon fixation and emission reduction in microalgae through efficient spectral transmission. Or ref. [16] designed a photobioreactor incorporating internal optical-fiber illumination to enhance light distribution uniformity and productivity, demonstrating a 43% increase in biomass for Spirulina platensis and a 38% increase for Scenedesmus dimorphus compared with a control.

In this study, two commercially available optical fibers, "Thorlabs' 0.22 NA TECS hard-clad" and "CeramOptec's Optran Ultra WFGE", were evaluated for their spectral transmittance and attenuation under clear-sky and cloudy-sky conditions modeled with the SPD imported from Section 2.1. Table 2 and Figure 2 summarize the properties of the selected fibers and illustrate the wavelength-dependent attenuation of cables, respectively.

Table 2. Summary of Selected Optical Fibers.

Name	Operating Wavelength	Operating Temperature	Source
Thorlabs' 0.22 NA TECS hard-clad	250–1200 nm	−60 to 125 °C	[23]
Optran Ultra WFGE	400–2400 nm	−190 to 350 °C	[24]

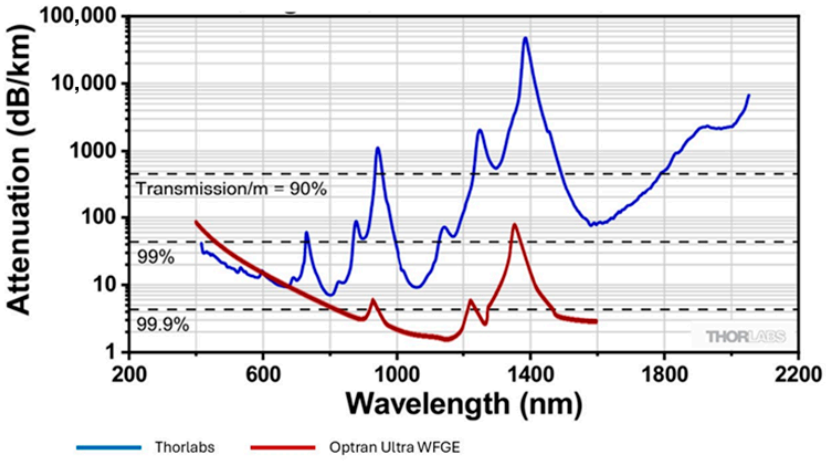


Figure 2. Wavelength-dependent attenuation of Thorlabs and Optran Ultra WFGE fibers.

The optical performance of the fibers was evaluated in terms of attenuation (α), expressed as spectral power loss per unit length [25]. Using Equations (1)–(3), the attenuation

spectra were converted into transmittance spectra by applying the exponential decay relation for each wavelength, assuming uniform loss along the fiber length.

$$P_{out}(\lambda) = \frac{P_{in}(\lambda)}{10^{\propto(\lambda)\frac{L}{10}}} \quad (1)$$

$$T = \frac{P_{out}}{P_{in}} \quad (2)$$

$$T = 10^{-\propto L/10}(db/km) \quad (3)$$

where P_{out} is output power, P_{in} is input power, L is the length of the optical fiber, T is the transmittance, and α is the attenuation coefficient.

The impact of the optical fibers on the transmitted light was considered by multiplying the fiber transmittance at each wavelength by the incident solar SPD, yielding the transmitted SPD at the fiber output. This approach enables simultaneous consideration of the spectral characteristics of both the fiber material and the solar source, providing a realistic representation of the light available for algal cultivation. For this study, a fiber length of 70 m was assumed, corresponding to the vertical and horizontal distance required to route daylight from the rooftop solar collector to the PBR floor in the four-story building model. This cable length directly influences total transmittance through the exponential attenuation relation and was used consistently across all SPD, PPFD, and DLI calculations.

The calculated SPDs were numerically integrated across the PAR range (400–700 nm) to determine the unweighted PAR ($W \cdot m^{-2}$) (Equation (4)). PAR represents the portion of solar radiation that can be used for photosynthesis and corresponds to approximately 43% of the total energy in the standard AM1.5 solar spectrum [26].

$$PAR = \int_{400}^{700} E(\lambda)d\lambda \left(W \cdot m^{-2}\right) \quad (4)$$

where $E(\lambda)$ is the spectral irradiance ($W \cdot m^{-2} \cdot nm^{-1}$).

The photosynthetic photon flux density (PPFD) ($\mu mol \cdot m^{-2} \cdot s^{-1}$) was calculated from the transmitted spectral irradiance by converting radiant energy to photon flux at each wavelength, followed by numerical integration over the photosynthetically active radiation (PAR) waveband (400–700 nm) using a wavelength-dependent energy–photon conversion factor [27]. As indicated in Equation (5), PPFD quantifies the rate at which photosynthetically active photons reach a surface and represents the total light intensity available for photosynthesis.

$$PPFD = 10^6 \sum_{\lambda=400}^{700} E(\lambda) \cdot \frac{\lambda}{hcN_A} \cdot \Delta\lambda (\mu mol \cdot m^{-2} \cdot s^{-1}) \quad (5)$$

where N_A is Avogadro's constant and is equal to 6.022×10^{23} (mol^{-1}), h is Planck's constant and is equal to 6.626×10^{-34} ($J \cdot s$), c is the speed of light and equals 3×10^8 ($m \cdot s^{-1}$), and λ is the effective wavelength.

Finally, the daily light integral (DLI) ($mol \cdot m^{-2} \cdot d^{-1}$), representing the total number of photons received during the photoperiod, was obtained by multiplying the PPFD by the daylight duration in seconds and converting to moles.

$$DLI = PPFD \times Daylength \times 10^{-6} \left(mol \cdot m^{-2} \cdot d^{-1}\right) \quad (6)$$

This sequential approach, which integrates SPD to obtain PAR, converts to PPFD, and accumulates over daylight hours to calculate DLI, yields unweighted values when no biological weighting is applied. In other words, if the effective action spectra of the

microalgae are not considered, the results represent the total available light energy across the PAR range, independent of species-specific absorption characteristics. However, as illustrated in Figure 3 the light absorption and photosynthetic efficiency of microalgae vary considerably across species, primarily due to differences in pigment composition and cellular structure.

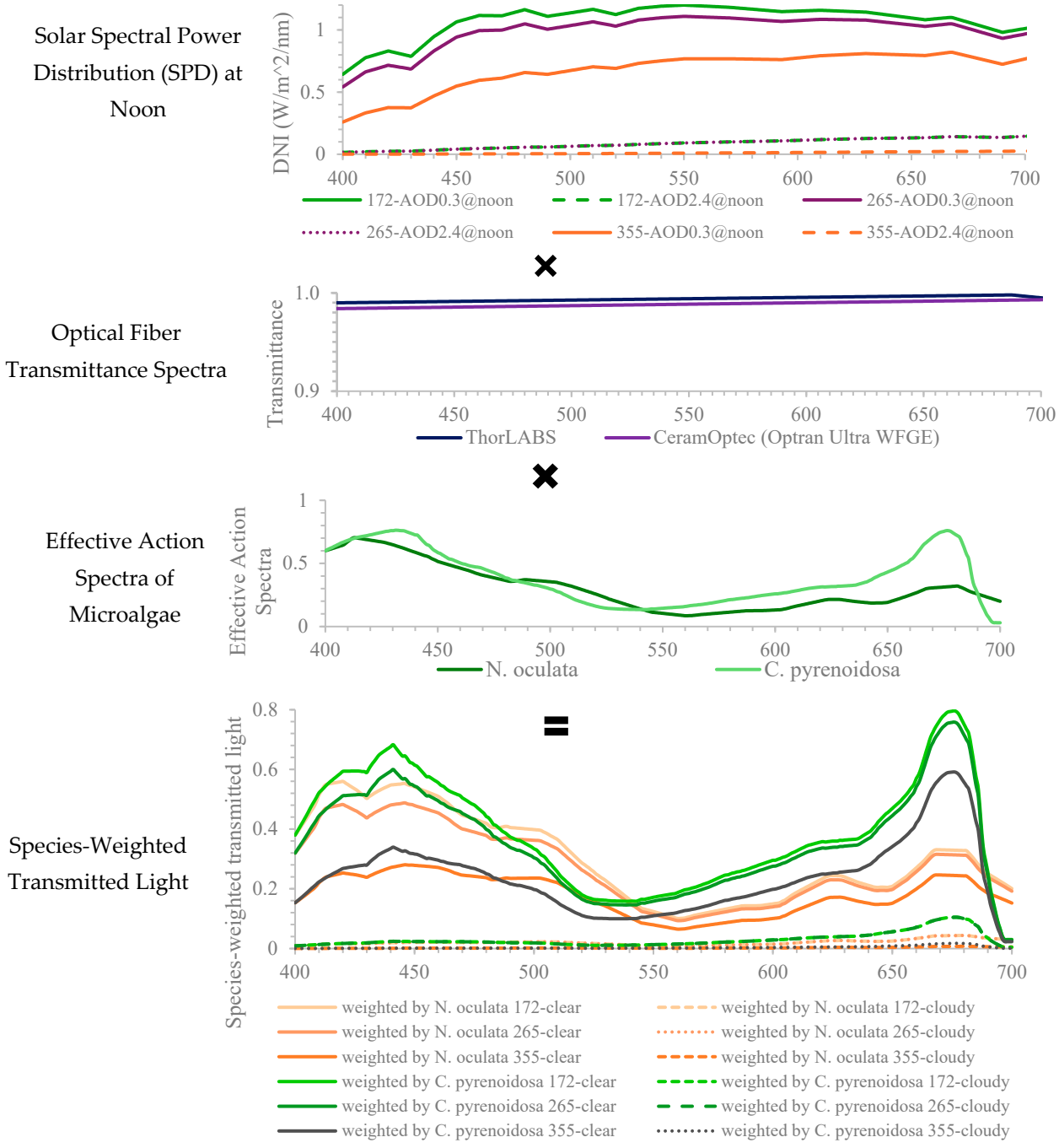


Figure 3. Process of generating species-weighted transmitted light from solar spectra, fiber transmittance, and algal action spectra.

Consequently, the effective action spectrum, which represents the efficiency of light in driving photosynthesis, also differs among species. This spectrum is defined as the product of the absorption spectrum, indicating the proportion of light absorbed at each wavelength, and the photosynthetic action spectrum, which characterizes the relative quantum efficiency of photosynthesis across wavelengths [28]. As a result, the effective

action spectrum serves as a wavelength-dependent weighting function for quantifying the effectiveness of absorbed light in photosynthetic energy conversion.

Two widely studied microalgae, *Nannochloropsis oculata* and *Chlorella pyrenoidosa*, were selected for their availability of high-resolution effective action spectra and for their differing pigment compositions. As listed in Equation (7), weighted irradiance was obtained by multiplying the transmitted SPD at each wavelength by the species' normalized effective action spectrum:

$$E_{weighted}(\lambda) = E(\lambda) \times S_{eff}(\lambda) \quad (7)$$

where $E(\lambda)$ is the transmitted spectral irradiance ($W \cdot m^{-2} \cdot nm^{-1}$), and $S_{eff}(\lambda)$ is the normalized effective action spectrum of the species.

It should be noted that, for the energy simulation, *Chlorella vulgaris* was selected due to its well-documented cultivation parameters and widespread use in indoor PBR systems. However, *C. vulgaris* lacks a high-resolution effective action spectrum suitable for wavelength-specific spectral weighting. Therefore, *Chlorella pyrenoidosa*, which exhibits closely similar spectral absorption behavior and shares the same chlorophyll a–b pigment system, was adopted as a proxy species for spectral weighting.

In addition, *Nannochloropsis oculata*, characterized by a distinct pigment composition and spectral response, was included to evaluate species-dependent sensitivity to the transmitted SPD. Accordingly, the effective action spectra of *C. pyrenoidosa* and *N. oculata* were used as representative species to perform a species-informed spectral evaluation. *N. oculata*, a eustigmatophyte, contains chlorophyll a but lacks chlorophyll b and exhibits strong absorption in the blue–green region (400–550 nm) due to its high carotenoid content (e.g., violaxanthin). In contrast, *C. pyrenoidosa*, a chlorophyte, contains both chlorophyll a and chlorophyll b, resulting in broader absorption peaks in the blue (~430–480 nm) and red (~640–680 nm) spectral regions. These two species therefore represent contrasting pigment systems and photosynthetic strategies.

Importantly, *C. pyrenoidosa* and *C. vulgaris* share the same chlorophyll a–b pigment system and exhibit substantial overlap in absorption behavior across the photosynthetically active radiation (PAR) range (400–700 nm). While C. pyrenoidosa typically shows slightly enhanced red-region absorption associated with its pyrenoid-rich chloroplast structure, and *C. vulgaris* exhibits marginally broader blue–green absorption related to carotenoid composition, comparative pigment studies [29,30] confirm substantial overlap in their dominant absorption bands. Consequently, *C. pyrenoidosa* provides a biologically representative proxy for *C. vulgaris* in the spectral weighting analysis.

Based on these considerations, species-weighted PAR, PPFD, and DLI were computed using the effective action spectra of *C. pyrenoidosa* and *N. oculata*, and the results are interpreted as a species-based sensitivity evaluation of how fiber-transmitted SPD aligns with different photosynthetic pigment systems.

Figure 4 illustrates the workflow for generating species-weighted transmitted light for a 1-m optical fiber configuration. The top figure shows the transmitted daylight SPDs for the three representative days, followed by the measured transmittance spectra of the optical fiber. The fiber exhibits nearly constant, high transmittance across the 400–700 nm range, so its influence is minimal. In contrast, the effective action spectra of *N. oculata* and *C. pyrenoidosa* exhibit substantial wavelength-dependent variation, meaning that the interaction between the daylight SPD and the species-specific action spectra is the primary determinant of the species-weighted PAR, PPFD, and DLI. As shown in the bottom figure, applying the action spectra to the transmitted SPDs yields species-weighted transmitted light distributions that capture the actual photosynthetically usable radiation available to each organism.

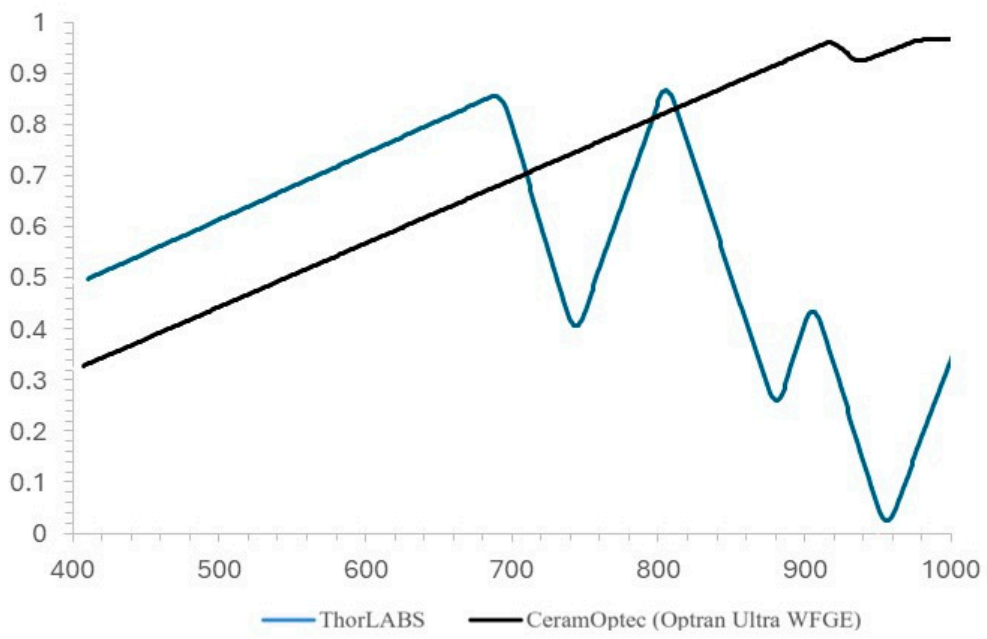


Figure 4. Spectral Transmittance of Optical Fibers.

As explained in Section 2.2, to obtain annual PPFD, DLI, and fiber-delivered energy, the year was divided into three representative solar periods: the summer solstice, the winter solstice, and the equinox (shared by spring and fall). For each representative day, hourly spectral irradiance was generated using the Bird Simple Spectral Model, and the corresponding DNI values were computed under both clear-sky and cloudy-sky conditions. The classification of clear versus cloudy hours was determined from the EPW weather file by evaluating hourly total sky cover; the resulting seasonal cloudiness ratios were then applied to the corresponding seasonal period to weight clear- and cloudy-sky contributions when deriving the annual values. Annual totals were reconstructed by assigning 91.25 days to each solstice period and 182.5 days to the combined spring–fall equinox, and then summing the seasonally weighted daily values. Using this approach (Equation (8)), full-year fiber-optic performance was estimated accurately without requiring a full 8760-h simulation.

$$\begin{cases} E_d = (1 - r_d)\, E_{d,clr} + r_d\, E_{d,cld} \\ E_{annual} = \sum \omega_d E_d \end{cases} \quad (8)$$

where $E_{d,clr}$ is the daily value under clear sky conditions for the representative day d. $E_{d,cld}$ is the daily value under cloudy sky conditions for the representative day d; r_d is the fraction of cloudy hours for period d, and ω_d is the number of days represented by period d in the annual cycle.

In addition to fiber length and sky cloudiness, as discussed in Section 2.1, snow cover and low ambient temperatures may also contribute to transmittance losses during winter conditions. According to the EPW weather file for State College, the minimum recorded outdoor temperature is −17 °C. This temperature remains within the manufacturer-specified operating range for the optical fibers evaluated (Table 2), so no additional temperature-induced optical transmission losses were considered in this case study. Although low temperatures can make materials more brittle, these effects are more likely to affect mechanical durability than intrinsic optical transmittance, so they are not considered in the present optical performance analysis.

Regarding snow cover, attenuation effects were estimated following the snow optical behavior reported in ref. [31]. Given the average winter snow depth in State College (~2.65 cm) and the reported rapid attenuation within the first few centimeters of snow, an

effective visible-light transmittance factor of 0.65 was applied to the winter-season portion of the calculations to account for snow-induced losses on the collectors.

In addition to environmental effects, transmittance losses also result from system-level optical inefficiencies throughout the daylight delivery chain. Specifically, the performance of the primary collector, secondary optical elements, and diffuser can affect the amount of light delivered. These representative optical efficiency ranges were adopted based on reported component efficiencies in the literature [19] 0.50–0.91 for the collector, 0.89–0.93 for secondary optics, 0.9–0.98 for the heat filter, and 0.85–0.92 for the diffuser. As these efficiencies are system-dependent, their product was used as an overall system-level optical multiplier in the sensitivity analysis. Three scenarios were evaluated by selecting low, mid, and high values within the reported ranges, resulting in overall multipliers of η_opt, non-fiber = 0.76 (optimistic), 0.53 (baseline), and 0.34 (conservative), which were uniformly applied to the final calculated outputs.

2.3. LED-Equivalent Energy Calculation for PV and Fiber Systems

To quantify the contribution of solar technologies to the lighting demands of the PBR system, two parallel energy-equivalent pathways were evaluated: a. solar-fiber delivered optical energy, and b. solar-PV generated electrical energy for LED lighting. Both calculations were performed annually, and the resulting values were normalized to LED-equivalent energy to allow direct comparison of the fiber and PV pathways.

a. Annual Solar-Fiber Optic to Photon Conversion

For the fiber system, the annual photon flux delivered to the PBR plane, $\Phi_{\text{fiber.annual}}$, was obtained from Section 2.2 using the three-period seasonal approach (clear-, cloudy-weighting, species weighting, and SPD→PAR→PPFD→DLI transformation). Because the fiber delivers optical energy directly, the equivalent amount of electricity that LEDs would require to generate the same photon quantity was calculated by Equation (9).

$$\mathrm{E_{LED.equ.}} = \frac{\Phi_{\text{fiber.annual}}}{\eta_{\text{LED}}} (\mathrm{J{\cdot}year^{-1}}) \tag{9}$$

where η_{LED} is the photon efficacy, which in modern horticultural LEDs typically ranges from 2.6–3.5 μmol·J^{-1}; in this study, the assumed value is 3 μmol·J^{-1}. $E_{LED.equ.}$ known as LED-equivalent energy or avoided LED energy, this value represents electrical lighting energy that the system does not need because fibers provide usable daylight. This allows both systems, PV-driven LEDs and fiber-delivered daylight, to be quantitatively compared using unified biological performance metrics.

b. Annual PV Electricity to Photon Conversion

Annual PV electricity generation was estimated using the same three representative solar days described in Section 2.1 (summer solstice, equinox, winter solstice). For each day, direct normal irradiance (DNI) was obtained from the Bird Simple Spectral Model under both clear- and cloudy-sky conditions and weighted using the seasonal cloud-cover ratios extracted from the EPW weather file. The resulting seasonally weighted irradiance values were converted into annual solar energy using the day-count factors of 91.25 days for each solstice and 182.5 days for the combined spring–fall equinox period. The annual solar energy available to PV modules, $\mathrm{E_{solar.annual}}$, as then converted to annual PV electricity output using a representative module conversion efficiency of 18%, reflecting commercially available rooftop crystalline-silicon modules:

$$\mathrm{E_{PV.annual}} = \eta_{\mathrm{PV}} \mathrm{E_{solar{\cdot}annual}} \left(\mathrm{J{\cdot}year^{-1}}\right) \tag{10}$$

where η_{PV} = 0.18 is the PV conversion efficiency.

Next, to express PV-generated electricity in biologically comparable terms, the PV electricity was converted into photon-equivalent LED output using the same LED efficacy.

2.4. System Integration and PBR Space Energy Simulation

To assess the influence of lighting source, solar availability, and system effectiveness on the integrated system's overall energy and biological performance, two operational configurations were developed in EnergyPlus.

- Basement PBR system: supported by optical fiber systems and PV systems.
- Rooftop PBR system: supported by daylight and PV systems.

Regarding the PBR implementation and its setting layout, the flat-panel PBR configuration was adopted, featuring a culture depth of 0.1 m enclosed within a total module thickness of 0.2 m to accommodate tubing connections and routine maintenance. Each panel was installed vertically, with dimensions of 2 m in height and 1 m in width, and spaced 1 m apart between adjacent rows to ensure accessibility for operation and service. The resulting effective floor footprint per unit was 1.2 m^2.

For energy simulation, a four-story residential building model (DOE/ASHRAE prototype) was implemented in EnergyPlus to evaluate the annual heating, cooling, and lighting energy demands under each scenario. The building, located in State College, PA (40.8° N, 77.9° W), features a typical mid-rise apartment configuration with four conditioned floors and a total floor area of 2824.2 m^2 (30,400 sq ft), with 706.1 m^2 (7600 sq ft) per floor. Based on this floor plan, each PBR-integrated floor corresponds to a total culture volume of 117.6 m^3 for 588 PBR panels. Following ref. [18], a biomass productivity of 0.8 g L^{-1} day^{-1} was assumed for *C. vulgaris* under these operating conditions, resulting in an estimated daily biomass output of 94 kg day^{-1} per PBR floor. In the scenario where the PBR floor is located in the basement, the full rooftop area (700 m^2, 7535 sq ft) was utilized for PV installation, and an additional 1 m^2 solar-concentrating collector was installed on the roof to support the ThorLABS fiber-optic daylighting system weighted with *C. pyrenoidosa*. In contrast, when the PBRs are located on the rooftop, only half of the roof surface (350 m^2, 3767 sq ft) remains available for PV installation due to space competition with the cultivation system.

Two distinct EnergyPlus models were developed to represent the scenarios described above. In each model, a single floor was designated for photobioreactor (PBR) integration, while the remaining floors were modeled as residential zones. Annual heating, cooling, and lighting energy demands for the PBR-integrated floor were obtained using EnergyPlus simulations. The energy outputs of the optical fiber and photovoltaic (PV) systems were calculated externally using the previously described methods and applied as offsets to the EnergyPlus-derived lighting and electrical energy demands to determine the reported net results.

Table 3 summarizes the EnergyPlus building model and HVAC system configuration. For each scenario, the temperature and light intensity on the PBR-integrated floor were maintained at 25 °C and 200 μmol m^{-2} s^{-1}, respectively. The optical and thermal properties of the greenhouse covering used in the rooftop scenario, including U-value, Solar Heat Gain Coefficient (SHGC), and Visible Transmittance (T-vis), are provided in Table 4. All reported energy results correspond solely to the PBR-integrated floor, as the analysis compares system-level energy performance.

Table 3. Building model and HVAC system summary in the EnergyPlus model.

Parameter	Value
Number of Floors	4
Exterior walls Construction	Steel-frame walls (2 × 4, 16 in o.c.) 0.4 in. stucco + 5/8 in. gypsum board + wall Insulation + 5/8 in. gypsum board
Roof Construction	Built-up roof roof membrane + roof insulation + metal decking
Total Conditioned area (ft^2) per floor	7600
Total Conditioned area (ft^2)	30,400
HVAC System Type	Packaged rooftop air conditioner
Fan Control	Constant volume
Cooling Type	Direct expansion
Heating Type	Fossil fuel furnace

Table 4. Optical and thermal properties of the rooftop greenhouse covering.

Glazing Type	U-Value (W/m^2K)	SHGC	T-Vis
Double-layer Polyethylene (two 6 mil PE layers with 13 mm air gap)	2.464	0.786	0.782

3. Results

3.1. Optical Fiber Transmission and Photosynthetically Active Metrics

As explained in Section 2.2 the transmittance of the two fiber-optic cables evaluated in this study (Thorlabs silica fiber and CeramOptec Optran Ultra WFGE) was calculated using the attenuation coefficients provided by each manufacturer and an assumed cable length of 70 m, accounting for both vertical and horizontal distortion.

Figure 5 depicts the spectral transmittance calculated for two 70 m-long cables. Considering the spectral transmittance across the visible range (400–700 nm), which is critical for photosynthetic activity in microalgae, both fibers exhibit moderate transmittance. The Thorlabs cable exhibits approximately 0.2 higher transmittance throughout this region, indicating reduced attenuation and more efficient delivery of biologically relevant light to the PBR surface. Beyond 700 nm, the Thorlabs fiber shows pronounced attenuation features. In contrast, the CeramOptec fiber demonstrates smoother, more monotonic transmission behavior across the full 400–1000 nm spectrum.

Although spectral differences exist outside the PAR band, both cables maintain the overall shape and continuity of the solar spectrum within the 400–700 nm range. Some wavelength-dependent attenuation occurs, especially near the red-edge region; however, the transmitted spectra retain the essential PAR characteristics required for photosynthesis. These findings suggest that fiber-transmitted daylight remains photosynthetically effective for microalgal cultivation in PBR-integrated systems.

To quantitatively assess the transmitted spectral energy, three complementary metrics, PAR, PPFD, and DLI, were employed. The stepwise conversion from solar SPD to PAR, PPFD, and ultimately DLI allowed for a consistent comparison of unweighted and species-weighted photosynthetic potentials. Unweighted PAR values describe the total radiative energy transmitted through the optical fibers, while PPFD and DLI provide biologically

relevant indicators of photosynthetic usability. When weighted using the effective action spectra of *N. oculata* and *C. pyrenoidosa*, the results revealed that both species achieve peak photosynthetic efficiency in the blue (430–480 nm) and red (640–680 nm) regions, with moderate attenuation in the green band due to lower chlorophyll absorption. These findings are consistent with established photosynthetic response profiles for green microalgae and validate the spectral selectivity of the optical fiber daylighting system for biological applications. As described in Section 2.2. PAR, PPFD, and DLI were derived by computing spectrally resolved irradiance for three representative seasonal days (summer solstice, equinox, and winter solstice), weighted by seasonal cloudiness fractions obtained from the EPW file and scaled by the number of days in each season. The resulting seasonal totals were converted to annual values and then divided by 365 to obtain the daily averages. In addition, three system-level performance scenarios were defined using different non-fiber optical efficiency assumptions (optimistic, baseline, and conservative). Table 5 reports the resulting daily average PAR, PPFD, and DLI at the fiber output for both fiber types under all three scenarios. These daily averages provide a consistent basis for comparing unweighted and species-weighted light availability delivered by the two optical fiber systems.

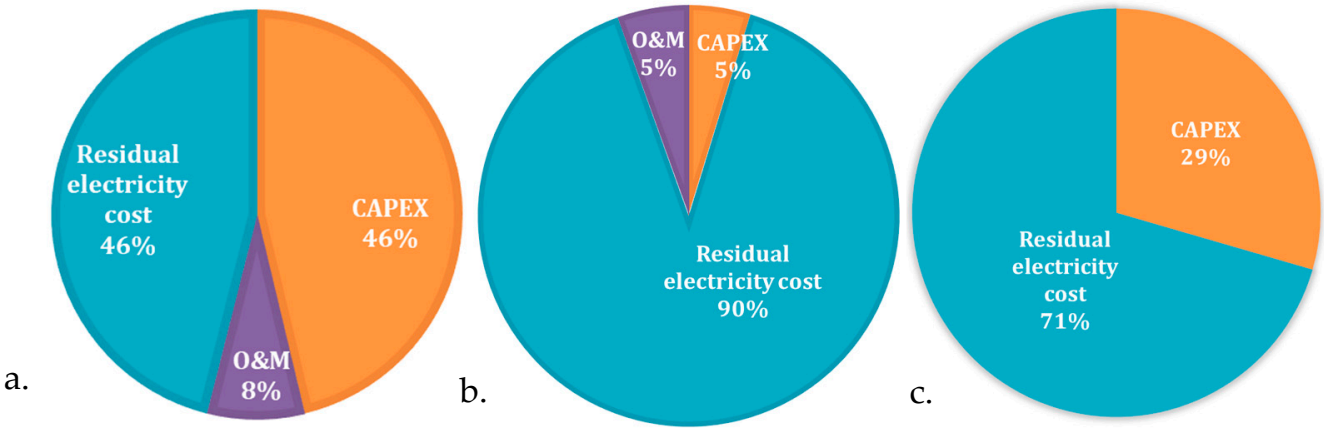


Figure 5. Annualized cost breakdown: (**a**) PV-supported basement PBR system, (**b**) Fiber-optic-assisted basement PBR system, (**c**) Rooftop greenhouse PBR system.

Table 5 shows that the ThorLABS fiber consistently delivers higher unweighted PAR, PPFD, and DLI compared with the CeramOptec fiber. This advantage persists after applying species-specific weighting functions for *N. oculata* and *C. pyrenoidosa*, reflecting the ThorLABS fiber's stronger transmittance across the PAR band. For *C. pyrenoidosa*, whose absorption spectrum extends strongly into the red region, the weighted PPFD and DLI are notably higher, indicating that this species benefits more from the preserved red-region transmission characteristics. In contrast, *N. oculata*, whose pigment system is dominated by blue-green absorption, receives proportionally less usable photon flux due to its narrower effective action spectrum. Overall, the fiber-based daylight transport provides meaningful photosynthetically active light to the PBR, and the relative magnitudes between fibers and species align with their known pigment compositions and spectral absorption characteristics. Based on this consistent performance advantage, the ThorLABS fiber was selected for subsequent system-level analyses.

Table 5. Daily average PAR, PPFD, and DLI at the fiber output for ThorLABS and CeramOptec fibers (area-normalized per 1 m^2). Results include 70 m fiber attenuation and a winter snow-cover reduction factor of 0.65, with additional non-fiber optical losses applied via scenario-specific system efficiency multipliers η = 0.76 (optimistic), 0.53 (baseline), and 0.38 (conservative).

	Optimistic Scenario		**Baseline Scenario**		**Conservative Scenario**	
	ThorLABS	CeramOptec	ThorLABS	CeramOptec	ThorLABS	CeramOptec
Unweighted PAR ($Wh \cdot m^{-2}.day^{-1}$)	516.4	389.0	361.2	272.1	230.4	173.5
Unweighted PPFD ($\mu mol \cdot m^{-2} \cdot s^{-1}$)	179.2	136.0	125.4	95.1	80.0	60.7
Unweighted DLI ($mol \cdot m^{-2} \cdot d^{-1}$)	8.9	6.8	6.2	4.7	4.0	3.0
Species-weighted PAR—*N. oculate* ($Wh \cdot m^{-2}.day^{-1}$)	133.7	99.0	93.5	69.2	59.6	44.2
Species-weighted PPFD—*N. oculate* ($\mu mol \cdot m^{-2} \cdot s^{-1}$)	44.3	33.1	31.0	23.2	19.7	14.8
Species-weighted DLI—*N. oculate* ($mol \cdot m^{-2} \cdot d^{-1}$)	2.2	1.7	1.5	1.2	1.0	0.7
Species-weighted PAR—*C. pyrenoidosa* ($Wh \cdot m^{-2}.day^{-1}$)	184.7	138.0	129.2	96.5	82.4	61.5
Species-weighted PPFD—*C. pyrenoidosa* ($\mu mol \cdot m^{-2} \cdot s^{-1}$)	63.8	48.1	44.6	33.6	28.5	21.4
Species-weighted DLI—*C. pyrenoidosa* ($mol \cdot m^{-2} \cdot d^{-1}$)	3.2	2.4	2.2	1.7	1.4	1.1

3.2. System Performance Analysis

To evaluate the feasibility of supplying the lighting energy required by the PBR-integrated building floor, two solar-based strategies were examined: (1) direct photovoltaic (PV electricity generation, and (2) fiber-optic daylight transport. These systems differ fundamentally in their mechanisms of energy delivery. PV converts incident solar radiation to electricity to power LED luminaires. In contrast, the fiber system directly channels spectrally usable daylight to the PBRs with minimal electro-optical conversion losses. Because each system interacts differently with seasonal solar availability, optical losses, and architectural constraints such as rooftop area or vertical routing, a comparative performance assessment is necessary to identify realistic design pathways for achieving net-zero or reduced lighting energy demand.

In this section, a quantitative analysis of both approaches was conducted using representative climate conditions for State College, PA. The PV-based assessment estimates the system capacity required to fully offset the annual electrical lighting load, accounting for sensitivity to photoperiod, LED efficacy, and peak-sun-hour variability. In parallel, the fiber-optic assessment evaluates the PAR, PPFD, and DLI that can be delivered through optical fibers, accounting for collector size, attenuation, cable length, and species-specific action spectra. By quantifying the effective contribution of each system and identifying its govern-

ing constraints, this comparative framework establishes the practical limits and integration opportunities for solar-driven illumination in PBR-equipped building environments.

a. PV System Performance

Analysis of the solar resource for State College, PA, using three representative annual dates under both clear- and cloudy-sky conditions, indicates that rooftop PV generation can theoretically offset the full lighting demand of the PBR-integrated floor. Using the modeled PBR configuration (588 flat-panel reactors, 2 m^2 illuminated area each, 200 $\mu mol \cdot m^{-2} \cdot s^{-1}$ target intensity), the instantaneous lighting electrical load is approximately 78 kW, or approximately 133 W per reactor, resulting in approximately 940 $kWh \cdot day^{-1}$ for a 12-h photoperiod and 1250 $kWh \cdot day^{-1}$ for a 16-h photoperiod.

When converted to PV system size using typical regional peak-sun-hour (PSH) values for State College (4 $PSH \cdot day^{-1}$), the PV array required to balance the PBR lighting demand is 235 kWDC for the 12-h case and 314 kWDC for the 16-h case. Applying a conservative PSH range (3.5–4.5 $h \cdot day^{-1}$) produces corresponding capacity ranges of 209–269 kWDC (12 h) and 279–358 kWDC (16 h). This translates to approximately 1360–2330 m^2 of required rooftop area, assuming 6.5 m^2 per kWDC for crystalline-silicon modules. To generalize scalability, these results can be normalized per reactor. The required PV capacity is approximately 0.35–0.46 kWDC per reactor for the 12-h case and 0.47–0.61 kWDC per reactor for the 16-h case, providing a practical metric for preliminary PV sizing across different building applications. Because winter daylight durations in State College shorten to less than 10 h, a portion of the lighting demand must be supplied after sunset. Therefore, limited electrical storage, equivalent to 2–4 h of nighttime lighting reserve, or approximately 0.25–0.45 kWh per reactor, is beneficial to mitigate seasonal variability and maintain continuous lighting operation without relying on grid imports.

LED photon efficacy strongly influences the sizing requirement. Lower efficiencies (e.g., 2.5 $\mu mol \cdot J^{-1}$) increase the PV capacity to 0.43–0.55 kWDC per reactor, whereas high-performance LEDs (e.g., 3.5 $\mu mol \cdot J^{-1}$) reduce the requirement to 0.30–0.39 kWDC per reactor. Photoperiod length, urban rooftop availability, and targeted grid independence further contribute to variation around the optimal design point.

Overall, a PV installation sized at approximately 0.40–0.55 kWDC per reactor, supplemented by a short-duration storage buffer, represents an appropriate design target for achieving an annual net-lighting-energy balance in PBR-integrated buildings located in climates similar to State College, PA.

b. Fiber System Performance

The contribution of fiber-delivered daylight to PBR lighting demand was assessed by converting species-weighted PPFD values to DLI, and then translating this photon flux into equivalent electrical energy using an LED photon efficacy of 3 $\mu mol \cdot J^{-1}$. The rationale for considering this efficacy was to maintain consistency with the PV sizing analysis, which used 3 $\mu mol \cdot J^{-1}$. The calculated daily electrical-equivalent energy was annualized and scaled to the total illuminated PBR floor area (1176 m^2). Using this methodology, the ThorLABS fiber weighted with *C. pyrenoidosa* delivers approximately 0.13, 0.21, and 0.3 $kWh \cdot m^{-2} \cdot day^{-1}$ of LED-equivalent lighting energy under conservative, baseline, and optimistic scenarios, respectively. When applied to the full cultivation footprint, this results in approximately 156, 244.1, and 348.9 $kWh \cdot day^{-1}$, respectively, of offset lighting energy, or 57–127 $MWh \cdot yr^{-1}$. All reported values are normalized to a 1 m^2 solar collector area and account for fiber attenuation, routing losses, snow-cover reduction, and system-level optical inefficiencies.

Relative to the modeled electrical lighting demand of the PBR floor (940–1250 $kWh \cdot day^{-1}$), fiber-delivered daylight offsets approximately 12–37% of the total daily lighting energy,

depending on scenario. Achieving complete electrical lighting offset with fiber-based daylighting alone would require approximately 3170–9442 m^2 across scenarios, which substantially exceeds the rooftop area needed for an equivalently sized photovoltaic system. This analysis demonstrates that, although fiber-delivered daylight can significantly reduce lighting energy demand and offer spectral and spatial advantages, it is not competitive with photovoltaic systems in terms of area required for bulk electrical energy generation.

The feasibility of a compact photobioreactor (PBR) system depends heavily on the selected microalgal species and their corresponding spectral weighting functions. As summarized in Table 5 and Figure 3 which present the effective action spectra of representative microalgae, *C. pyrenoidosa* shows approximately a 40–45% greater effective photosynthetic response than *N. oculata*. Consequently, species with greater spectral responsiveness exhibit higher photosynthetic productivity under equivalent irradiance. Therefore, species selection directly affects both system sizing requirements and the potential reduction in electrical lighting demand.

Beyond species-dependent effects, optical transmittance losses increase with fiber length, making the vertical placement of the cultivation floor a critical design consideration, especially when daylight distribution spans multiple stories. For instance, for the ThorLABS fiber assessed in this study, extending the cable length from 25 m to 70 m results in an approximate 33.1% decrease in average optical transmission. Thus, the spatial configuration between the solar collector and the PBR, particularly the total routing distance, is a primary factor influencing overall system efficiency. To establish a conservative upper bound for routing-related losses, this study deliberately placed the PBR in the basement, representing a worst-case deployment scenario and ensuring that the reported performance estimates remain robust for practical applications.

3.3. Whole PBR System Space's Energy Consumption Impacts

As explained in Section 2.2 and the above solar system analyses, two scenarios were simulated in EnergyPlus to evaluate the overall energy performance with the integration of the PBR system. In the rooftop scenario, the cultivation light requirement was assumed to be met by artificial lighting and through direct solar exposure transmitted through greenhouse coverage. In contrast, the basement scenario relied entirely on artificial illumination supported by the optical fiber systems. The building energy simulation results for these two scenarios are presented in Table 6. It should be noted that at this point, the overall energy demand was estimated through the simulation, and the contributions of the PV or solar fiber systems were not included.

Table 6. The total space annual energy demand of the PBR system for different scenarios.

	Space Energy Demand (GJ)			
Scenario	**Heating**	**Cooling**	**Lighting**	**Total**
PBR System in the Basement	0	804.8	977.4	1782.2
PBR System in the Rooftop Greenhouse	9.3	770.2	623.8	1403.3

Table 6 shows the annual heating, cooling, lighting, and total energy demand for the entire floor (basement or rooftop) where the PBR system is located, based on two scenarios. Overall, in both scenarios, the lighting energy demand is too high because the artificial lighting is provided to meet the PBR system's photosynthetic lighting energy needs. The rooftop-integrated PBR scenario shows lower lighting energy demand. Direct access to daylight in rooftop-integrated PBR reduces artificial lighting requirements by

~36% compared with the basement PBR system. Continuous LED operation, due to the high lighting energy demand, generates substantial internal heat gains that significantly increase the cooling energy demand in both scenarios.

Based on Table 6, the heating energy demand was overall low in both scenarios, reaching zero in the basement PBR scenario. It is because of the substantial waste heat and internal gains generated by LED operation and PBR systems. In other words, the space-heating energy requirements were met by internal gains, so the HVAC system had little need to provide additional heating.

Without any active solar-based technologies (i.e., PV or fiber-optic daylighting), the two scenarios exhibited comparable heating and cooling demands; however, the rooftop-integrated PBR configuration achieved approximately 21% lower total annual energy use than the basement-integrated system due to its direct access to daylight. Photovoltaic and fiber-optic solar systems could fully offset the lighting energy demand of the basement PBR system if sufficient solar collection area were available. Based on the collector-normalized performance reported in Section 3.2, achieving a complete lighting offset in the basement scenario requires approximately 3200 m^2 of solar collector area dedicated to fiber-optic daylight delivery and 1500 m^2 of PV surface area.

In contrast, the rooftop-integrated PBR scenario, despite benefiting from direct daylight, still required approximately 380.8 GJ of grid electricity annually to meet its residual lighting demand under the available roof-area constraints. Under these area constraints, the resulting total annual energy use of the PBR-integrated floor is approximately 804.8 GJ for the basement scenario and 1160.3 GJ for the rooftop scenario.

4. Discussion

4.1. Applicability in Cold Climate: Potential and Limitations

The present study's results suggest that incorporating solar-assisted lighting strategies, via rooftop PV or fiber-optic daylight delivery, can significantly offset the intensive lighting demand associated with building-integrated PBR systems. However, the performance and feasibility of these strategies should not be solely determined by energy considerations. Seasonal solar availability, reduced winter photoperiods, and architectural constraints related to building form and roof utilization strongly influence both the achievable energy savings and the associated capital and operating costs. As a result, a comparative assessment that jointly considers energy performance and economic implications is essential for evaluating the applicability of solar-assisted PBR systems in cold regions. Three PBR integration strategies were examined in this study: (i) a rooftop greenhouse configuration, (ii) a basement-integrated PBR system supported by PV-power, and (iii) a basement-integrated PBR system supplemented by fiber-optic daylight delivery.

For the rooftop greenhouse PBR configuration, the total system cost is governed by the greenhouse construction capital cost and the annual electricity cost required to meet the PBR-related remaining energy demand, after accounting for direct daylight access. In contrast, basement-integrated PBR systems were evaluated under two solar-assisted strategies. In the first case, PBR lighting demand is supported through PV-powered LED illumination, and total cost includes PV and storage capital costs, annual operation and maintenance (O&M), and grid electricity expenditures required to meet the remaining PBR energy demand. In the second case, fiber-optic daylight delivery is integrated to supplement LED lighting for the PBR system. The total cost in this configuration includes the capital costs of the solar collector, tracking system, coupling optics, and fiber-optic cabling, as well as electricity expenditures to meet the remaining needs of the PBR system. Table 7 summarizes the cost ranges considered for each system component and its corresponding data sources. It should be noted that these cost values were compiled from

published literature and manufacturer data spanning 2018–2025; therefore, results should be interpreted as approximate, rather than precise life-cycle costs.

Table 7. Cost assumptions used for PV- and fiber-assisted PBR system evaluation.

Item	Cost	Source
Electricity rate (State College, PA, USA)	\$/kWh	[32]
PV system CAPEX	1.47 \$/WDC	[33]
Annual PV O&M	13–25 $\$\cdot kWDC^{-1}\cdot yr^{-1}$	[34]
Battery storage CAPEX	192 \$/kWh	[35]
Greenhouse construction CAPEX	20–50 $\$/ft^2$	[36]
Solar concentrator CAPEX	150–250 $\$\cdot m^2$	[37]
Solar tracker CAPEX	0.08–0.1 \$/W	[38]
Solar-to-fiber coupling optics & housing CAPEX	500–2000 \$	[39]
Fiber optic cable CAPEX	27.45 $\$\cdot m^{-1}$	[23]
Fiber optic O&M	2% of fiber cable CAPEX$\cdot yr^{-1}$	[40]
PBR cultivation module O&M	0.55–1.41 $\$\cdot m^{-2}\cdot yr^{-1}$	[41]
PBR cleaning O&M	0.12–0.37 $\$\cdot m^{-2}\cdot yr^{-1}$	[41]

All capital cost estimates were converted to equivalent annual costs over a 25-year system lifetime using a capital recovery factor (CRF = 0.071), corresponding to a real discount rate of 5%, to account for the time value of money. For parameters reported as ranges, the midpoint was used in the analysis.

For the basement PBR supported by PV, the installed PV system CAPEX was estimated at \$403,515, which corresponds to an equivalent annual CAPEX of \$28,630 yr^{-1} when annualized over a 25-year lifetime using a capital recovery factor (CRF = 0.071, 5% real discount rate). Annual PV operation and maintenance costs were estimated at \$5216 yr^{-1}, while battery storage CAPEX of \$39,514 contributed an additional \$2804 yr^{-1} when annualized. Combined with the remaining grid electricity expenditure of \$31,298 yr^{-1}, the total annual cost of the basement PV-supported PBR configuration was estimated at \$67,947 yr^{-1}.

For the basement PBR supported by fiber-optic daylighting, capital costs included the solar collector (\$800), tracking system (\$360), coupling optics and housing (\$1500), and fiber-optic cabling (\$20,588), yielding a total fiber system CAPEX of \$23,248. Annualized using the same CRF, this corresponds to an annual CAPEX of \$1649 yr^{-1}. In addition, PBR-specific operation and maintenance costs, including cultivation module maintenance and cleaning, amounted to \$1441 yr^{-1}, while fiber-system O&M was conservatively estimated at \$465 yr^{-1}. Together with the residual grid electricity cost of \$31,298 yr^{-1}, the total annual cost of the fiber-assisted basement PBR configuration was estimated at \$34,388 yr^{-1}, substantially lower than the PV-only basement scenario.

In the rooftop greenhouse PBR configuration, system costs were primarily determined by greenhouse construction CAPEX and electricity costs. The greenhouse capital cost was estimated at \$266,000, corresponding to an annualized CAPEX of \$18,873 yr^{-1} using the same CRF. Combined with an annual electricity cost of \$45,123 yr^{-1} to meet the PBR lighting demand, the total annual cost of the rooftop greenhouse configuration was estimated at \$63,996 yr^{-1}. Figure 5 presents the annualized cost breakdowns for the three PBR integration scenarios evaluated in this study.

These cost results highlight an essential trade-off between energy performance and economic feasibility. Although rooftop integration and expanded solar collection strategies can substantially reduce artificial lighting demand, reductions in energy consumption do not necessarily translate into lower total system cost. In the rooftop greenhouse configuration, direct access to daylight reduces reliance on electric lighting; however, the additional capital investment in greenhouse construction and supporting structural systems dominates overall expenditures. Similarly, achieving a complete lighting offset through rooftop PV requires increased generation capacity and supplemental energy storage in cold climates to address seasonal daylight limitations, resulting in higher system complexity and upfront cost.

In contrast, basement-integrated PBR systems supported by fiber-optic daylight delivery exhibit a more favorable cost-energy balance. While fiber-optic systems incur additional capital costs related to solar collectors, tracking systems, coupling optics, and long-distance fiber transmission, these costs remain modest relative to the capital requirements of greenhouse construction or large-scale PV deployment. As a result, the fiber-assisted basement configuration achieves meaningful reductions in grid electricity use while maintaining substantially lower annualized costs than both the PV-only basement system and the rooftop greenhouse configuration. These findings underscore a critical design insight: strategies that maximize solar energy capture and daylight availability may minimize operational energy demand, but they are not necessarily economically optimal once capital costs and architectural constraints are considered.

4.2. Potentials of Solar-Assisted PBR Integration

The fiber-optic daylighting system demonstrated the most economically favorable performance, achieving comparable energy offsets at less than 50% the annualized cost of PV-supported and rooftop greenhouse alternatives. Furthermore, delivering photosynthetically useful light directly to the cultivation space without introducing additional internal heat gains is particularly advantageous during summer and shoulder seasons, when reductions in lighting-related heat loads can lower cooling demand. In cold climates, although waste heat from LED lighting can benefit space heating during peak winter conditions, fiber-optic systems still improve overall thermal performance during periods when heating is not required. While, in an optimal scenario, fiber-optics require 2.3 times more surface area than a PV-integrated system, this concern could be addressed by reducing the distance between the collector and the diffusers. As discussed in the Section 3.2, increasing the length of the cable form has a substantial impact on the reduction of the transmittance.

PV systems, when appropriately sized, can offset the full annual PBR lighting demand even under modest peak-sun-hour conditions. With sufficient rooftop area and grid interconnection, PBR-integrated floors can, in theory, achieve net-zero lighting energy consumption in cold climates, particularly when PV generation is complemented by short-duration energy storage.

4.3. Limitations and Cold-Climate Design Constraints

Cold climates impose several limitations on the performance of solar-assisted PBR systems. Reduced daylight hours, low solar angles, frequent cloud cover, and increased heating loads strongly influence both PV electricity generation and fiber-optic daylight availability. Consequently, system sizing must be based on winter worst-case conditions to ensure reliable year-round operation. For PV-supported systems, short winter photoperiods and low irradiance necessitate oversized PV arrays and substantial energy storage to maintain nighttime cultivation, increasing spatial requirements and capital costs. Although fiber-optic daylight delivery reduces internal heat gains from artificial lighting, it does not

provide the incidental heating benefits associated with LED waste heat during the coldest months. As a result, the relative benefit of fiber-optic daylighting in winter may be lower than in warmer seasons.

Overall, these findings emphasize the importance of evaluating solar-assisted PBR systems through a combined energy-economic lens. In cold-climate contexts, hybrid solutions that strategically supplement artificial lighting rather than fully replace it may offer the most cost-effective and architecturally viable pathway for integrating high-intensity PBR systems into buildings.

4.4. Potential Improvement Directions

Based on the final results of this study, several technology and design development pathways emerge. These can be grouped into two main themes: optical fiber and daylight system development and building-scale integrated system design, including thermal, lighting, or structural, and urban constraints.

4.4.1. Optical Fiber and Daylight System Development

While the fiber-optic daylight system proved highly spatially efficient, further advances in fiber glass or polymer design optimized explicitly for photosynthetic applications could enhance performance. For example, fibers with enhanced red-band transmittance, lower attenuation over longer runs, and optimized coupling with rooftop collectors, such as tracking concentrators, would improve the overall delivered light to the PBR. Research into novel fibers [42,43] suggest the potential for improved daylight transfer systems.

Incorporating adaptive daylight control systems, such as solar-tracking mechanisms, dichroic spectral filters, or variable coupling interfaces, could enable the fiber network to respond dynamically to seasonal variations and avoid both over- and under-illumination. Such adaptive controls would simultaneously optimize energy use and stabilize cultivation productivity by maintaining photosynthetically appropriate light levels.

The development of hybrid concentrator-fiber systems capable of capturing and transmitting higher-flux daylight during low-sun or cloudy conditions represents another promising direction. Integrating Fresnel lens collectors or compound parabolic concentrators with fiber bundles could significantly increase delivered quantum flux, particularly in winter. Literature on daylight fiber systems [19] similarly emphasizes the need for improvements in optical efficiency, spectral transmission, and cost reduction to support broader architectural deployment.

4.4.2. Building-Scale Integrated System Design

Given that lighting energy dominates the operational profile of PBR systems and that LED waste heat substantially increases the cooling load, future research must address the heating-cooling synergy within the building. Strategies such as recovering waste heat from the cultivation process for space heating, integrating heat-recovery ventilation, or coupling the PBR with low-temperature hydronic heating loops may offer meaningful reductions in winter heating demand. In cold-climate applications where heating loads become dominant, system optimization should therefore extend beyond lighting efficiency to include comprehensive thermal energy management. In dense urban environments or high-rise buildings, fiber-optic daylighting systems should be located as close as possible to the diffusers to minimize routing distance and avoid the need for enlarged collector surface areas in spatially constrained settings. Future design frameworks could leverage vertical daylight distribution through shared fiber bundles, light shafts, or atrium-based routing to supply multiple floors from a compact rooftop collector. In contrast, PV installations may be constrained by shading from surrounding buildings or structural loading limits. These considerations highlight the importance of integrating solar-assisted lighting strategies

within broader architectural and urban design contexts to maximize the feasibility of PBR deployment in space-constrained settings. For new construction, the placement of PBR systems can become a strategic design decision. Integrating the PBR floor during early architectural planning enables building designers to ensure adequate daylight access, minimal fiber routing distances, and optimal collector orientation, while also providing the necessary structural and spatial provisions for fiber distribution networks. Because daylight availability and cable length strongly affect system performance, early-stage integration can significantly enhance the overall efficiency and reliability of fiber-assisted illumination. Regulatory and zoning considerations also play an essential role, particularly in cold-climate regions where building envelopes are tightly sealed and highly insulated. The addition of a PBR floor, with substantial internal heat gains from cultivation equipment and supplemental lighting, must be carefully coordinated with HVAC capacity, facade insulation, and daylight routing strategies to prevent unintended overheating or excessive cooling loads. These factors underscore the need for a holistic design approach that aligns daylight harvesting, thermal performance, and architectural constraints to ensure a high-performing building-integrated PBR system.

5. Conclusions

This work quantified the feasibility of using rooftop photovoltaic systems and solar light-guiding fibers to offset the substantial lighting energy demand of building-integrated microalgae PBRs in cold climates. The optical modeling results confirm that the ThorLABS fiber delivers photosynthetically meaningful photon flux across seasonal sky conditions, with the *C. pyrenoidosa* weighting yielding ~0.21 kWh·day^{-1} per 1 m^2 solar collector of LED-equivalent energy. PV analysis demonstrated that 0.40–0.55 kWDC per reactor is sufficient to achieve a net-lighting-energy balance for a whole PBR floor, provided sufficient rooftop area is available. System-level building simulations further revealed that rooftop-integrated PBR deployment reduces total annual space energy demand by ~21% relative to a basement configuration due to enhanced daylight access and reduced cooling loads. When solar technologies are integrated with sufficient surface area, the basement PBR scenario becomes fully lighting-energy-neutral. At the same time, the rooftop greenhouse configuration retains a grid reliance of 380.8 GJ due to limited roof space for PV capacity.

Overall, the results show that solar-assisted PBR systems are technically viable in cold-climate buildings and can substantially improve energy performance if rooftop area, daylight access, and fiber routing are optimized. While fiber-optic daylighting achieves approximately half the annualized cost of PV-supported systems, it requires a larger collector surface area, on the order of twice that of PV. In contrast, PV systems scale more directly with available area, whereas fiber-optic system sizing is additionally influenced by routing distance and species-dependent spectral response. The comparative analysis further indicates that reductions in lighting energy demand do not necessarily correspond to lower total system cost, as additional capital investments associated with greenhouse construction or expanded PV capacity can outweigh operational energy savings. It should be noted that the present analysis is based on modeled spectral irradiance using the BIRD model and representative-day weighting, rather than on site-specific measured spectral data, and therefore, the results should be interpreted as relative performance trends rather than absolute predictions. Future work should address seasonal variability, incorporate local or long-term measured irradiance data for validation, and explore optical collector optimization and heating–cooling energy coupling to further enhance full-building integration and carbon-negative operation.

Author Contributions: Conceptualization, N.G.A. and J.W.; Methodology, N.G.A., M.E. and J.W.; Software, M.E.; Validation, N.G.A. and J.W.; Formal analysis, N.G.A. and J.W.; Investigation, M.E. and

J.W.; Data curation, N.G.A. and J.W.; Writing—original draft, N.G.A., M.E. and J.W.; Writing—review & editing, N.G.A. and J.W.; Visualization, N.G.A.; Supervision, J.W. All authors have read and agreed to the published version of the manuscript.

Funding: This research was funded by the USDA-NIFA-147360.

Data Availability Statement: The original contributions presented in this study are included in the article. Further inquiries can be directed to the corresponding author.

Conflicts of Interest: The authors declare no conflicts of interest.

References

1. Chen, L.; Huang, L.; Hua, J.; Chen, Z.; Wei, L.; Osman, A.I.; Fawzy, S.; Rooney, D.W.; Dong, L.; Yap, P.-S. Green construction for low-carbon cities: A review. *Environ. Chem. Lett.* **2023**, *21*, 1627–1657. [CrossRef]
2. Metwally, W.M.; Ibrahim, V.A.R. The integration of bio-active elements into building façades as a sustainable concept. *Buildings* **2024**, *14*, 3086. [CrossRef]
3. Yaman, Y.; Tokuç, A.; Deniz, İ.; Ezan, M.A.; Köktürk, G.; Dalay, M.C.; Demirel, Z. Photobioreactor facade panels: Enhancing comfort, reducing energy use, and capturing carbon in temperate continental climates. *Syst. Microbiol. Biomanuf.* **2025**, *5*, 357–370. [CrossRef]
4. Pruvost, J.; Cornet, J.-F.; Pilon, L. Large-Scale Production of Algal Biomass: Photobioreactors. In *Algae Biotechnology*; Springer: Cham, Switzerland, 2016; pp. 41–66.
5. Chisti, Y. Biodiesel from microalgae. In *Biotechnology Advances*; Elsevier: Amsterdam, The Netherlands, 2007; Volume 25, pp. 294–306.
6. Kang, D.; Kim, K. Real wastewater treatment using a moving bed and wastewater-borne algal–bacterial consortia with a short hydraulic retention time. *Processes* **2021**, *9*, 116. [CrossRef]
7. Zittelli, G.C.; Rodolfi, L.; Bassi, N.; Biondi, N.; Tredici, M. Photobioreactors for microalgal biofuel production. In *Algae for Biofuels and Energy*; Springer: New York, NY, USA, 2013; pp. 225–266.
8. Patel, A.K. Microalgae in Dual Role: An Effective Platform for Biological Carbon Capturing and High Value Carotenoid Production. *Curr. Pollut. Rep.* **2025**, *11*, 34. [CrossRef]
9. Talaei, M.; Mahdavinejad, M.; Azari, R.; Prieto, A.; Sangin, H. Multi-objective optimization of building-integrated microalgae photobioreactors for energy and daylighting performance. *J. Build. Eng.* **2021**, *42*, 102832. [CrossRef]
10. Nguyen, T.D.; Le, H.T.H.; Khoo, K.S.; Bui, H.M. Algae windows: A novel approach towards sustainable building design and energy conservation. *Pol. J. Environ. Stud.* **2024**, *33*, 3243–3255. [CrossRef]
11. Zhang, J.; Tsamis, A.; Rosenberg, D. Algae bio-reactive building envelope: Dynamic lighting and energy aspects for algae-based building skin. In Proceedings of the 2022 Building Performance Analysis Conference and SimBuild Co-Organized by ASHRAE and IBPSA-USA, Chicago, IL, USA, 14–16 September 2022.
12. Arora, R.; Sudhakar, K.; Rana, R.S. Photobioreactors for building integration: A overview of designs and architectural potential. *Heliyon* **2024**, *10*, e35168. [CrossRef] [PubMed]
13. Hijazi, R.M.; Mounsef, J.R.; Kanaan, H.Y. Comparison of light intensity effect on microalgal growth in cactus-like and cylindrical photo bioreactors. *Processes* **2020**, *12*, 1664. [CrossRef]
14. Sukačová, K.; Lošák, P.; Brummer, V.; Máša, V.; Vícha, D.; Zavřel, T. Perspective design of algae photobioreactor for greenhouses—A comparative study. *Energies* **2021**, *14*, 1338. [CrossRef]
15. Pankratz, S.; Oyedun, A.O.; Kumar, A. Development of cost models of algae production in a cold climate using different production systems. *Biofuels Bioprod. Biorefin.* **2019**, *13*, 1246–1260. [CrossRef]
16. Xue, S.; Zhang, Q.; Wu, X.; Yan, C.; Cong, W. A novel photobioreactor structure using optical fibers as inner light source to fulfill flashing light effects of microalgae. *Bioresour. Technol.* **2013**, *138*, 141–147. [CrossRef]
17. NREL. Bird Simple Spectral Model, NREL. Available online: https://www.nrel.gov/grid/solar-resource/spectral (accessed on 3 November 2025).
18. Kosmopoulos, P.G.; Kazadzis, S.; Taylor, M.; Athanasopoulou, E.; Speyer, O.; Raptis, P.I.; Marinou, E.; Proestakis, E.; Solomos, S.; Gerasopoulos, E.; et al. Dust impact on surface solar irradiance assessed with model simulations, satellite observations and ground-based measurements. *Atmos. Meas. Tech.* **2017**, *10*, 2435–2453. [CrossRef]
19. Sreelakshmi, K.; Ramamurthy, K. Review on fibre-optic-based daylight enhancement systems in buildings. *Renew. Sustain. Energy Rev.* **2022**, *163*, 112514. [CrossRef]
20. Aslian, A.; Chong, K.-K.; Tavassoli, S.H.; Tan, C.-J.; Hazave, O.B. Rectangular glass optical fiber for transmitting sunlight in a hybrid concentrator photovoltaic and daylighting system. *Int. J. Photoenergy* **2020**, *2020*, 8813688. [CrossRef]

21. Onubogu, N.O.; Chong, K.-K.; Tan, M.-H. Review of Active and Passive Daylighting Technologies for Sustainable Building. *Int. J. Photoenergy* **2021**, *2021*, 8802691. [CrossRef]
22. Song, J.; Dessie, B.B.; Gao, L. Analysis and comparison of daylighting technologies: Light pipe, optical fiber, and heliostat. *Sustainability* **2023**, *15*, 11044. [CrossRef]
23. FG550UEC-0.22 NA, Ø550 µm Core Multimode Optical Fiber, High-OH for 250–1200 nm, TECS Double Clad, THORLABS. 2011. Available online: https://www.thorlabs.com/thorproduct.cfm?partnumber=FG550UEC (accessed on 4 January 2026).
24. High-Performance Fiber Solutions Optical Fibers & OEM Assemblies for UV, Sensing & Medical Applications, Ceram Optec. Available online: https://www.ceramoptec.com/products/fibers/optran-uvwfs.html (accessed on 4 January 2026).
25. Czerwinski, A.; Czerwinska, K. Statistical analysis of the photon loss in fiber-optic communication. *Photonics* **2022**, *9*, 568. [CrossRef]
26. Ringsmuth, A.K.; Landsberg, M.J.; Hankamer, B.D. Can photosynthesis enable a global transition from fossil fuels to solar fuels, to mitigate climate change and fuel-supply limitations? *Renew. Sustain. Energy Rev.* **2016**, *62*, 134–163. [CrossRef]
27. Zhen, S.; Kusuma, P.; Bugbee, B. Chapter 17—Toward an optimal spectrum for photosynthesis and plant morphology in LED-based crop cultivation. In *Plant Factory Basics, Applications and Advances*; Academic Press: New York, NY, USA, 2022; pp. 309–327.
28. Liining, K.; Dring, M.J. Action spectra and spectral quantum yield of photosynthesis in marine macroalgae with thin and thick thalli. *Mar. Biol.* **1985**, *87*, 119–129. [CrossRef]
29. Kroon, B.M.A.; Latasa, M.; Ibelings, B.W.; Mur, L.R. The effect of dynamic light regimes on Chlorella. *Hydrobiologia* **1992**, *238*, 71–78. [CrossRef]
30. Safafar, H.; Nørregaard, P.U.; Ljubic, A.; Møller, P.; Holdt, S.L.; Jacobsen, C. Enhancement of Protein and Pigment Content in Two Chlorella Species Cultivated on Industrial Process Water. *J. Mar. Sci. Eng.* **2016**, *4*, 84. [CrossRef]
31. Perovich, D.K. Light reflection and transmission by a temperate snow cover. *J. Glaciol.* **2007**, *53*, 201–210. [CrossRef]
32. Cost of Electricity in State College, PA, Energysage. 2025. Available online: https://www.energysage.com/local-data/electricity-cost/pa/centre-county/state-college/? (accessed on 16 December 2025).
33. SEIA-Solar Energy Industries Association. Solar Market Insight Report Q2 2025. 2025. Available online: https://seia.org/research-resources/solar-market-insight-report-q2-2025/ (accessed on 16 December 2025).
34. Wiser, R.H.; Bolinger, M.; Seel, J. Energy Markets & Planning-BERKELEY LAB. Benchmarking Utility-Scale PV Operational Expenses and Project Lifetimes: Results From a Survey of U.S. Solar Industry Professionals. 2020. Available online: https://emp.lbl.gov/publications/benchmarking-utility-scale-pv (accessed on 16 December 2025).
35. IRENA—International Renewable Energy Agency. Battery Energy Storage Systems: Key to Renewable Power Supply-Demand Gaps. 2025. Available online: https://www.irena.org/News/articles/2025/Aug/Battery-energy-storage-systems-key-to-renewable-power-supply-demand-gaps (accessed on 15 December 2025).
36. Vincent; HARNOIS Serres*Greenhouses. How Much Does a Commercial Greenhouse Cost? Available online: https://harnoisgreenhouse.com/commercial-greenhouse-cost/ (accessed on 16 December 2025).
37. Low-cost, G.G. Low-Cost, Lightweight Solar Concentrator. Available online: https://www.energy.gov/eere/solar/articles/low-cost-lightweight-solar-concentrator (accessed on 16 December 2025).
38. Bloch, E. Modernize. What Are the Pros and Cons of a Solar Tracker System? 2025. Available online: https://modernize.com/homeowner-resources/solar/solar-tracker-system-pros-cons (accessed on 16 December 2025).
39. Edmund—Optics | Worldwide. Mounted N-BK7 Corner Cube Retroreflectors. Available online: https://www.edmundoptics.com/f/optical-lenses/12462/ (accessed on 16 December 2025).
40. Tellus Venture Associates. *Cost Estimates for FTTP Network*; Tellus Venture Associates: Santa Cruz, CA, USA, 2015. Available online: https://www.tellusventure.com/downloads/santacruz/ctc_santa_cruz_ftth_estimate_may2015.pdf (accessed on 16 December 2025).
41. Zhu, Y.; Anderson, D.; Jones, S. *Algae Farm Cost Model: Considerations for Photobioreactors*; Pacific Northwest National Laboratory: Richland, WA, USA, 2018.
42. Asiabanpour, B.; Estrada, A.; Ramirez, R.; Downey, M.S. Optimizing natural light distribution for indoor plant growth using PMMA optical fiber: Simulation and empirical study. *J. Renew. Energy* **2018**, *2018*, 9429867. [CrossRef]
43. Maatallah, T.; Wahab, F.; Alzahrani, M.; Jamal, A.; Ali, S. Fiber optic daylighting with concentrating solar collectors: A state-of-the-art review. *Energies* **2025**, *18*, 2097. [CrossRef]

Disclaimer/Publisher's Note: The statements, opinions and data contained in all publications are solely those of the individual author(s) and contributor(s) and not of MDPI and/or the editor(s). MDPI and/or the editor(s) disclaim responsibility for any injury to people or property resulting from any ideas, methods, instructions or products referred to in the content.